nature biomedical engineering

ARTICLES

PUBLISHED: 19 DECEMBER 2016 | VOLUME: 1 | ARTICLE NUMBER: 0006

A transistor-like pH nanoprobe for tumour detection and image-guided surgery

Tian Zhao[1†], Gang Huang[1], Yang Li[1], Shunchun Yang[1], Saleh Ramezani[2], Zhiqiang Lin[1], Yiguang Wang[1], Xinpeng Ma[1], Zhiqun Zeng[1], Min Luo[1], Esther de Boer[3], Xian-Jin Xie[4], Joel Thibodeaux[5], Rolf A. Brekken[6], Xiankai Sun[2], Baran D. Sumer[7]* and Jinming Gao[1]*

It is challenging to detect a broad range of malignant tumours at high resolution, because of profound genetic and histological differences in cancerous tissue. Here, we report the design and performance of a fluorescent nanoprobe with transistor-like responses (transition pH = 6.9) for the detection of deregulated pH, which drives many of the invasive properties of cancer. The nanoprobe amplifies the fluorescence signal in the tumour over that in the surrounding normal tissues, resulting in a discretized, binary output signal with a spatial resolution smaller than 1 mm. The nanoprobe allowed us to image a broad range of tumours in mouse models using a variety of clinical cameras. We were able to perform real-time tumour-acidosis-guided detection and surgery of occult nodules (<1 mm³) in mice bearing head and neck or breast tumours, significantly lengthening mice survivability. We also show that the pH nanoprobe can be used as a reporter in a fast, quantitative assay to screen for tumour-acidosis inhibitors. The binary delineation of pH achieved by the nanoprobe promises to improve the accuracy of cancer detection, surveillance and therapy.

Cancer is a heterogeneous disease that displays diverse inter- and intra-tumoural genetic and phenotypic variations from non-transformed cells[1]. Molecular imaging of cancer-specific biomarkers offers the exciting opportunity for tumour detection at the earliest onset of disease and has rapidly advanced the preclinical and clinical development of a variety of imaging probes. Most common strategies have focused on cell-surface receptors such as folate receptor-α (ref. [2]), chlorotoxin[3], epidermal growth factor receptor (EGFR)[4], human epidermal growth factor receptor 2 (Her2/neu)[5] and tumour associated antigens (for example, prostate-specific membrane antigen)[6]. Although molecular diagnosis of these differences is useful to stratify patients towards personalized therapy, the ability to use the differences to diagnose a wide range of cancers is often not possible, because of genetic or phenotypic heterogeneity (for example, <25% of breast cancer patients have Her2/neu expression)[7,8]. In contrast to the diverse genotypes/phenotypes, deregulated energetics is a hallmark of cancer and represents a common pathway that is found in many types of cancer[9]. The best characterized alteration of energy metabolism in cancer cells is aerobic glycolysis (also known as the Warburg effect), where cancer cells preferentially take up glucose and convert it into lactic acid[10]. The clinical significance of the Warburg effect has been shown by the wide use of 2-deoxy-2-[^{18}F]fluorodeoxyglucose (FDG) in positron emission tomography (PET, >1.5 million annual procedures in the United States alone), which leverages the high glucose uptake of cancer cells[11].

Dysregulated pH, as a result of deregulated tumour metabolism, is emerging as another ubiquitous characteristic of cancer[12]. Cancer cells display a reversed pH gradient with a constitutively increased cytosolic pH and decreased extracellular pH (pH_e) compared with normal tissues regardless of their tissue origin and genetic background. The decreased pH_e, or tumour acidosis in the microenvironment[13,14], promotes extracellular-matrix remodelling and stimulates acid-activated proteases for increased local invasion and metastasis. Previously, we reported the development of a cyclo(Arg-Gly-Asp-D-Phe-Lys) (cRGDfK)-encoded, Cy5.5-conjugated pH-activatable nanoprobe to image solid tumours[15]. In this study, we simplified the previous nanoprobe design by removing the cRGDfK ligand and replacing the Cy5.5 dye with indocyanine green (ICG), a fluorophore approved for clinical use by the Food and Drug Administration (FDA) in the United States. The resulting pH-activatable ICG-encoded nanosensor (PINS) improved the sharpness of the pH response (for example, $\Delta pH_{10-90\%}$ decreased from 0.26 to 0.15) while allowing deeper fluorescence penetration in tissues, due to the longer wavelength of the ICG. PINS serves as a self-contained polymeric nanoprobe that acts as a 'chemical transistor' with a sharp on and off response that is analogous to the gating of electronic transistors (Fig. 1a). PINS was able to detect a variety of tumours using existing clinical cameras. Real-time, image-guided resection of established tumours and occult nodules (<1 mm³) in mouse models resulted in significantly improved long-term survival after cancer surgery. The ability of pH transistor nanoprobes to transform pH from an analogue biologic signal to a discrete exponentially amplified output radically alters the current imaging paradigm for cancer diagnosis, surveillance and therapy.

Design and synthesis of PINS

We synthesized a PINS nanoprobe consisting of poly(ethylene glycol)-*b*-poly(ethylpropylaminoethyl methacrylate) copolymers

[1]Department of Pharmacology, Simmons Comprehensive Cancer Center, University of Texas Southwestern Medical Center, OncoNano Medicine Inc., 5323 Harry Hines Boulevard, Y3.224, Dallas, Texas 75390, USA. [2]Department of Radiology, University of Texas Southwestern Medical Center, 5323 Harry Hines Boulevard, Dallas, Texas 75390, USA. [3]University Medical Center Groningen, Department of Surgery, Hanzeplein 1, 9713 GZ Groningen, Netherlands. [4]Department of Clinical Science, University of Texas Southwestern Medical Center, 5323 Harry Hines Boulevard, Dallas, Texas 75390, USA. [5]Department of Pathology, University of Texas Southwestern Medical Center, 5323 Harry Hines Boulevard, Dallas, Texas 75390, USA. [6]Department of Surgery, University of Texas Southwestern Medical Center, 5323 Harry Hines Boulevard, Dallas, Texas 75390, USA. [7]Department of Otolaryngology, University of Texas Southwestern Medical Center, 5323 Harry Hines Boulevard, Dallas, Texas 75390, USA. †Present address: OncoNano Medicine Inc., 5323 Harry Hines Boulevard Y.3224, Dallas, Texas 57390, USA. *e-mail: baran.sumer@utsouthwestern.edu; jinming.gao@utsouthwestern.edu

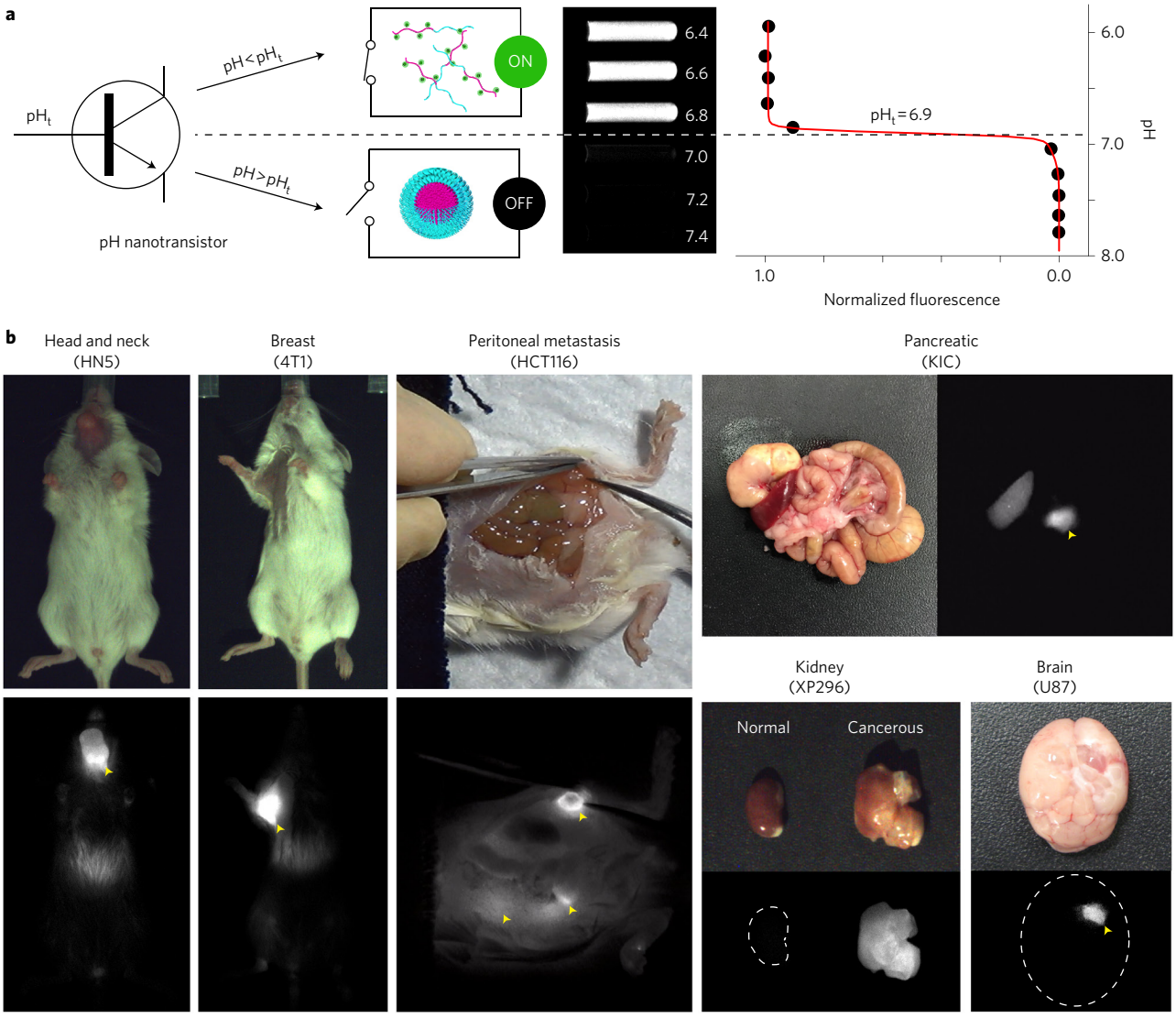

Figure 1 | pH transistor nanoprobes achieve broad tumour detection specificity. a, Schematic of pH nanotransistor with binary off/on response at a pH_t (threshold pH for fluorescence transition) of 6.9. At pH < 6.9, nanoprobes dissociate into protonated, highly fluorescent unimers (on state); at pH > 6.9, nanoprobes are silent (off state). **b**, PINS nanoprobes (intravenous injection given 24 h prior to imaging by SPY Elite clinical camera) demonstrate broad tumour imaging efficacy in a variety of tumour models (head and neck, breast, peritoneal metastasis, kidney, brain, pancreatic) and organ sites. Yellow arrowheads indicate the location of tumours. Additional tumour models are shown in Supplementary Fig. 5. *Ex vivo* quantification is available in Supplementary Fig. 6.

(PEG-*b*-P(EPA$_x$-*r*-ICG$_y$), where x and y indicate the number of repeating units of the EPA monomer and ICG dye, respectively; Supplementary Fig. 1). We systematically investigated the effect of polymer chain length and ICG density on the transition pH, sharpness of response, fluorescence activation ratio and diameter of the nanoprobes (Supplementary Tables 1 and 2). Increasing the repeating units of EPA from 40 to 120 resulted in sharper pH transitions ($\Delta pH_{on/off}$ decreased from 0.30 to 0.13) and slightly lower pH transitions (from 6.96 to 6.91). The particle diameter increased (20 to 30 nm) with the increase of PEPA length. ICG dye (excitation/emission wavelengths = 780/820 nm) was conjugated to the PEPA segment at different densities (averages of 0.5, 1.0 and 2.0 ICGs per polymer chain). A higher ICG conjugation number resulted in a sharper pH transition and higher fluorescence activation ratio. However, two ICGs per polymer chain also reduced the fluorescence intensity at pH 6.5 (on state) because of the increased formation of H-dimers, as indicated by a larger shoulder peak at 750 nm (Supplementary Fig. 1i). Based on these results, we chose PEG-*b*-P(EPA$_{100}$-*r*-ICG$_1$) as the optimal PINS composition (hydrodynamic diameter 26.0 ± 1.1 nm) for subsequent animal studies. A three-dimensional (3D) plot of fluorescence intensity as a function of pH and nanoprobe concentration illustrates the orthogonal pH-modulated fluorescence activation where the ICG signal was eliminated at blood pH (7.4) but dramatically activated at a lower pH (Supplementary Fig. 2a). Above pH 6.9, hydrophobic micellization and homo-fluorescence resonance energy transfer (homoFRET)-induced quenching[16] resulted in the annihilation of fluorescence. Below pH 6.9, PINS was dramatically activated, because of micelle dissociation into individual unimers, as supported by transmission electron microscopy (TEM) analysis (Supplementary Fig. 2c). The divergent protonated unimer and neutral micelle states[17] resembled the phase separation behaviours observed in p- and n-type semiconductors in electronic transistors (Supplementary Fig. 3)[18]. This binary (off/on) pH threshold sensor design is crucial to amplify the persistent but variable acidic tumour pH_e (6.5–6.9, average 6.84)[14], with signal suppression in blood (pH 7.4).

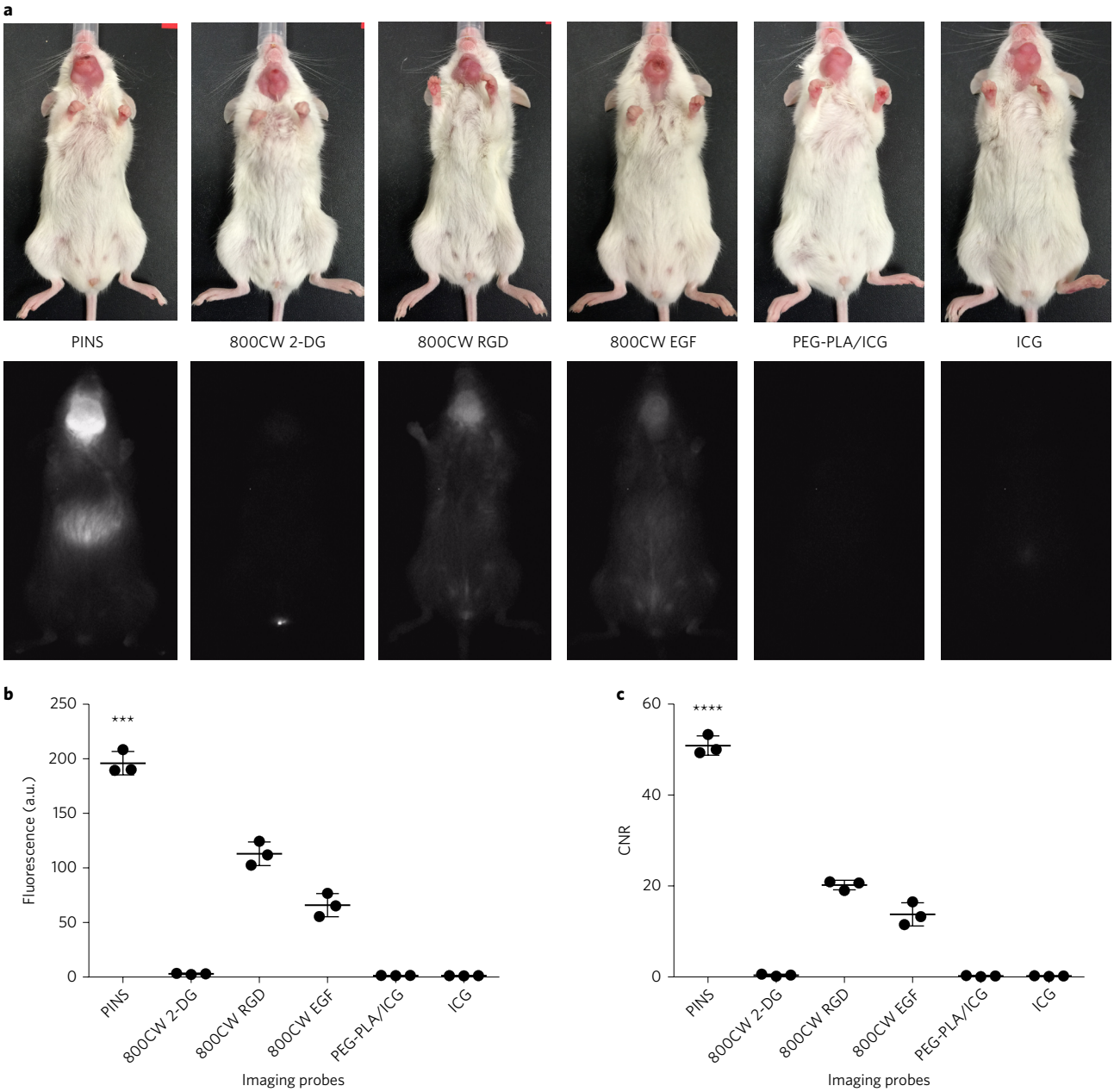

Figure 2 | Comparison between PINS and other commercial NIR probes. a, Images of mice bearing HN5 head and neck tumours 24 h after injection with different imaging probes. The fluorophore doses were the same for all groups. **b**,**c**, Quantification of the tumour fluorescence intensity (**b**) and contrast to noise ratio (**c**), demonstrating the superior imaging efficacy by PINS compared with the other imaging probes. Data are presented as mean ± s.d. ($n = 3$); ***$P < 0.001$, ****$P < 0.0001$, compared with other groups.

PINS achieves broad tumour detection accuracy

An initial dose-response study using a clinical SPY Elite camera established 2.5 mg kg^{-1} as the optimal dose of PINS, with a large contrast to noise ratio (CNR = 27) and a persistent time window (12–24 h) for detection in mice bearing human head and neck HN5 orthotopic tumours (Supplementary Fig. 4 and Supplementary Table 3). Besides HN5 tumours, we imaged additional orthotopic head and neck tumours (FaDu and HCC4034, the latter from a patient of B.D.S), a subcutaneous breast tumour (MDA-MB-231), an intramammary orthotopic breast tumour (triple negative 4T1), a peritoneal metastasis model from HCT116 colorectal cancer, a patient-derived xenograft (PDX) of kidney cancer, an orthotopic brain tumour from U87 glioma and two transgenic pancreatic ductal adenocarcinoma models (KIC and KPC). All non-transgenic tumours were established in non-obese diabetic-severe combined immunodeficiency (NOD-SCID) mice except 4T1 tumours in BalB/C mice. We observed bright tumour illumination across all tumour types (Fig. 1b and Supplementary Fig. 5). *Ex vivo* imaging revealed high contrast ratios of tumour over muscle (20- to 50-fold, Supplementary Fig. 6). Using the HN5 tumour model, we also demonstrated the compatibility of PINS with multiple clinical cameras (Supplementary Fig. 7). Comparison of PINS with other commercially available near-infrared (NIR) probes (800CW-conjugated 2-deoxy-D-glucose (2-DG), 800CW cRGD and 800CW EGF) at equivalent dye dose showed superior imaging efficacy with PINS (Fig. 2). ICG-loaded PEG-*b*-poly(lactic acid) (PEG-PLA/ICG) micelles and free ICG did not show observable tumour contrasts.

To investigate whether PINS can enhance the outcome of FDG–PET, we performed FDG–PET imaging in head and neck tumour-bearing mice followed by PINS imaging. In FDG–PET, brain, brown

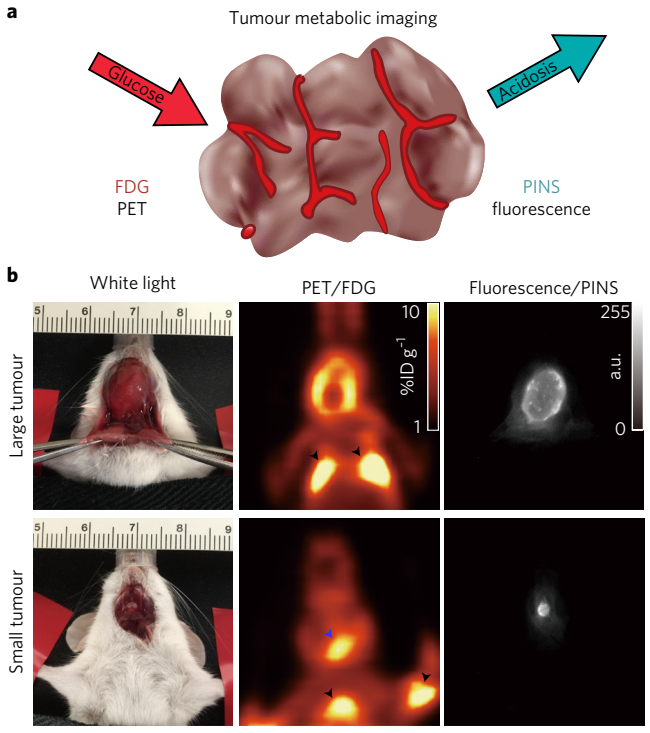

Figure 3 | PINS improves cancer detection compared with FDG–PET. **a**, Schematic of tumour metabolic imaging by PET with FDG versus NIR fluorescence imaging with PINS. **b**, SCID mice bearing large (200 mm^3) or small (10 mm^3) HN5 orthotopic tumours; PINS imaging showed improved sensitivity and specificity of tumour detection over FDG–PET. Black arrowheads and blue arrowheads indicate false positive detection of brown fat and striated muscle, respectively, in the PET images.

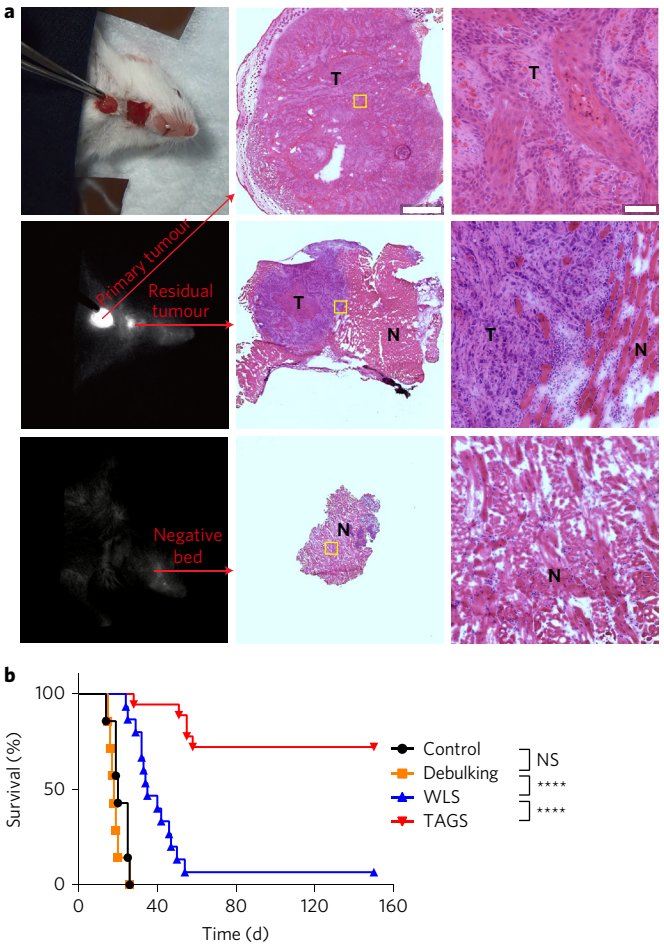

Figure 4 | TAGS in mice bearing orthotopic head and neck tumours. **a**, Surgical resection of primary HN5 tumours and successful detection of residual tumours using a SPY Elite camera. Visual inspection of the tumour bed was not able to differentiate residual tumours from surrounding muscle tissue (top left). Tumour tissue (T) and normal tissue (N) were verified by histology. Scale bar = 1 mm (low magnification) or 100 µm (high magnification). **b**, Debulking surgery provided no survival benefit compared with the untreated control. TAGS showed significantly improved long-term survival compared with WLS and other control groups (****$P < 0.0001$). For control and debulking group $n = 7$; for WLS group $n = 15$; for TAGS group $n = 18$. See Supplementary Videos for real-time surgical resection of HN5 tumours.

adipose tissues and other hypermetabolic tissues are known to avidly take up glucose resulting in false positives, a common problem with clinical PET (Supplementary Fig. 8)[19,20]. For tumour detection, although FDG–PET detected large HN5 tumours (~200 mm^3), it was not successful at detecting small tumour nodules (~10 mm^3, Supplementary Fig. 8b and Supplementary Table 4). In contrast, all tumour sizes were clearly visible by PINS, with a high CNR (> 20). *Ex vivo* signals for brain, brown adipose tissues, kidney or other FDG–PET-positive tissues were low (Supplementary Fig. 6). Furthermore, PINS was able to delineate tumour margins at sub-millimetre spatial resolutions (Fig. 3). These data suggest that PINS can be used as an adjuvant tool to improve the accuracy of tumour staging following FDG–PET. Due to the limitation of light penetration in tissues, PINS will be particularly useful in the imaging of superficial tumours, such as skin cancer or peritoneal metastasis (through a laparoscope).

We investigated the colocalization of PINS signals with tumour boundaries at the microscopic level (Supplementary Fig. 9a). HN5 tumour with green fluorescent protein (GFP)-labelled cancer cells and surrounding muscle tissues were collected as frozen sections (8 µm in thickness) 24 h after intravenous PINS injection. ICG fluorescence from PINS illustrated excellent overlap with GFP signals from HN5 cancer cells, which was further validated by haematoxylin and eosin (H&E) staining. To evaluate the contribution of dose accumulation on tumour contrast, we synthesized ^{3}H-labelled PINS through acetylation (-COCT$_3$) of the free amino groups in the copolymer[15]. At 24 h after ^{3}H-labelled PINS injection, tumour and normal muscle tissues were collected. Nanoprobe accumulation in tumour over normal tissues was highly variable between animals (two- to tenfold) as measured by ^{3}H radioactivity. In contrast, PINS fluorescence signals were able to discretize tumour versus normal tissues, because of signal amplification through pH activation (Supplementary Fig. 9b). Cellular imaging of activated PINS in HN5 tumour frozen sections further showed punctate signals inside cancer cells (Supplementary Fig. 9c), indicating nanoprobe internalization inside acidic subcellular organelles (for example, lysosomes) for sustained tumour contrast.

Tumour-acidosis-guided surgery by PINS improves survival

We performed real-time tumour-acidosis-guided surgery (TAGS) using the SPY camera in mice bearing HN5 head and neck or 4T1 breast cancers (Supplementary Videos 1 and 2). PINS (2.5 mg kg^{-1}) was injected intravenously 12–24 h before surgery. In a representative operation in HN5 tumour-bearing mice, after resection of the primary tumour, the residual tumour was clearly visible using the SPY camera (Supplementary Video 1 and Fig. 4a middle left panel), but not under white light (Fig. 4a top left panel). To validate the accuracy of margin delineation in a surgical setting, we performed

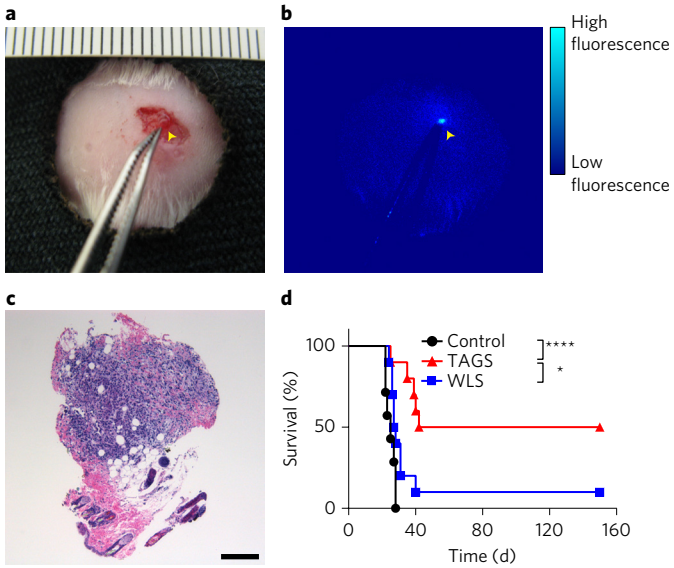

Figure 5 | Tumour-acidosis-guided surgery in mice bearing small occult breast tumour nodules. a,**b**, Tumour foci (< 1 million cells) were not distinguishable by visual detection (**a**), but were visible using the SPY camera (**b**). **c**, A representative histological section of a small breast tumour nodule resected during TAGS; scale bar = 200 µm. **d**, Kaplan–Meier curve demonstrates significantly improved long-term survival by TAGS compared with WLS and untreated control groups. For control groups $n = 7$; for WLS and TAGS groups $n = 10$; $^{*}P < 0.05$, $^{****}P < 0.0001$. See Supplementary Videos for real-time surgical resection of small occult breast tumours.

non-survival surgery in nine mice bearing HN5 head and neck tumours using a double blind protocol. The surgeon (B.D.S.) resected the tumours under PINS illumination and marked the tissue specimen (2–3 mm in size) as either primary tumour (fluorescence positive), tumour margin or tumour-negative muscle tissue (fluorescence negative) in the tumour bed. Frozen sections were made from all specimens, followed by H&E staining. Histological evaluation was performed independently by a surgical pathologist (J.T.) (Supplementary Fig. 10). PINS assessment accuracy was validated on all 27 tissue specimens by histologic interpretation; we observed a 100% confirmation rate (100% sensitivity and 100% specificity, Supplementary Table 5), with a 95% confidence lower boundary of 89.5%. Long-term survival surgery outcomes showed improved loco-regional control and overall survival with TAGS over white light surgery (WLS), debulking surgery and untreated controls (Fig. 4b). Debulking surgery with macroscopically positive margins typically provides no survival benefit for head and neck cancer and served as a control for the adequacy of WLS. WLS was superior to the debulking and untreated controls ($P < 0.0001$), indicating that it is an unbiased technique. TAGS led to the best outcome, with 13 out of 18 animals (72%) showing cures 150 d post-operatively ($P < 0.0001$ versus WLS, Fig. 4b and Supplementary Table 6).

To mimic clinical scenarios where identifying occult cancerous nodules is critical, we established small orthotopic breast tumours in immunocompetent female BalB/C mice. We injected 5×10^4 triple negative 4T1 breast cancer cells in the inguinal mammary pad. With an estimated doubling time of 24 h, the nodule size represented <1 million 4T1 cells in the foci on day 4. PINS under the SPY camera was able to identify the subcutaneous 4T1 foci through the skin, which was confirmed by histology (Fig. 5a–c). A tumour could not be detected at this stage through visual inspection or palpation. For the white light control, we allowed the tumour to grow to ~25 mm^3, so it was visible, and carefully resected the primary tumour and surrounding margin. TAGS (Supplementary Video 3) resulted in superior visualization, improving survival after resection over the untreated control and WLS ($P < 0.05$, Fig. 5d and Supplementary Table 6), demonstrating superb imaging sensitivity with PINS.

PINS facilitates screening of acidosis inhibitors

PINS was used to evaluate tumour response to small molecular inhibitors targeting different tumour acidosis pathways (Fig. 6). We selected four inhibitors: acetazolamide to target carbonic anhydrase IX (CAIX)[21], α-cyano-4-hydroxycinnamate (CHC) to target monocarboxylate transporter (MCT)[22], cariporide to target sodium proton exchanger 1 (NHE1)[23] and pantoprazole as a proton pump inhibitor (PPI)[24]. PINS was injected intravenously to SCID mice bearing HN5, 4T1 or human A549 lung tumour following inhibitor administration. NIR imaging 24 h after PINS injection showed that the greatest inhibition (50–80%) was achieved by the CAIX inhibitor acetazolamide over the phosphate-buffered saline (PBS) control in all three models. The other inhibitors showed less pronounced and more variable inhibitions in the tumour models. The PINS response is consistent with previously reported antitumour efficacy of CAIX inhibitors in tumour-bearing mice[25,26]. Compared with $^{1}H/^{31}P$ (ref. [27]) or hyperpolarization ^{13}C magnetic resonance imaging (MRI) methods[28], PINS imaging offers a simple and quantitative assay for the rapid screening of small molecular drugs targeting tumour acidosis pathways[21,29].

Pharmacokinetic and safety evaluations

To determine the pharmacokinetic and biodistribution profiles of PINS, we injected ^{3}H-labelled PINS at the same dose (2.5 mg kg^{-1}) as the imaging dose. The plasma concentration–time curve showed a two-phase behaviour over 24 h (Supplementary Fig. 12a). The α-phase half-life ($t_{1/2,\alpha}$) was 2.0 ± 1.6 h and the β-phase half-life ($t_{1/2,\beta}$) was 8.6 ± 2.7 h ($n = 4$). Biodistribution studies showed that tumour accumulation was 2.7 ± 1.9% of injected dose per gram (ID g^{-1}) of tissue. Liver and spleen were the main organs for PINS uptake.

A safety evaluation of PINS in immunocompetent C57BL/6 mice showed temporary body weight loss and an acute toxicity response at high doses (Supplementary Fig. 13a and Supplementary Table 7). The maximum tolerated dose was 250 mg kg^{-1}, 100-fold higher than the optimal imaging dose. Mice were given doses of 200 or 250 mg kg^{-1} PINS and sacrificed on days 1, 7 or 28. Liver and kidney functions were analysed (Supplementary Fig. 13b–e). Liver enzyme levels of alanine transaminase (ALT) and aspartate aminotransferase (GOT) increased on day 1 after PINS injection and returned to normal after seven days. Histologic analysis (Supplementary Fig. 14) showed microsteatosis in the liver in the 250 mg kg^{-1} group at day 1, but this returned to normal by day 28. Other major organs (for example, kidney, heart, spleen) were normal.

Discussion

Most cancer molecular imaging agents (for example, antibody-dye conjugates) rely on their binding to intended cancer targets to increase dose accumulation for observed tumour contrast. Such strategies translate the target concentration into a linearly proportional imaging signal. This analogue signal is subject to signal degradation and decreased signal to noise ratio (SNR) when amplified by increasing the dose or detector sensitivity. It can show great inter-test variability, because cancer target expressions are highly variable (for example, EGFR varies widely in head and neck tumours from 0.3- to 97-fold)[30], with spatial and temporal fluctuations. To overcome these limitations, we previously reported a signal amplification strategy that is orthogonal to dose accumulation through pH activation in response to angiogenic tumour vasculature and acidic extracellular pH[15]. In this study, we further clarified a pH transistor concept with a binary off/on response at a threshold pH (6.9) analogous to the electronic transistors with a threshold gating voltage (Supplementary Fig. 3). This transistor concept simplified the understanding of PINS function to switch and amplify variable

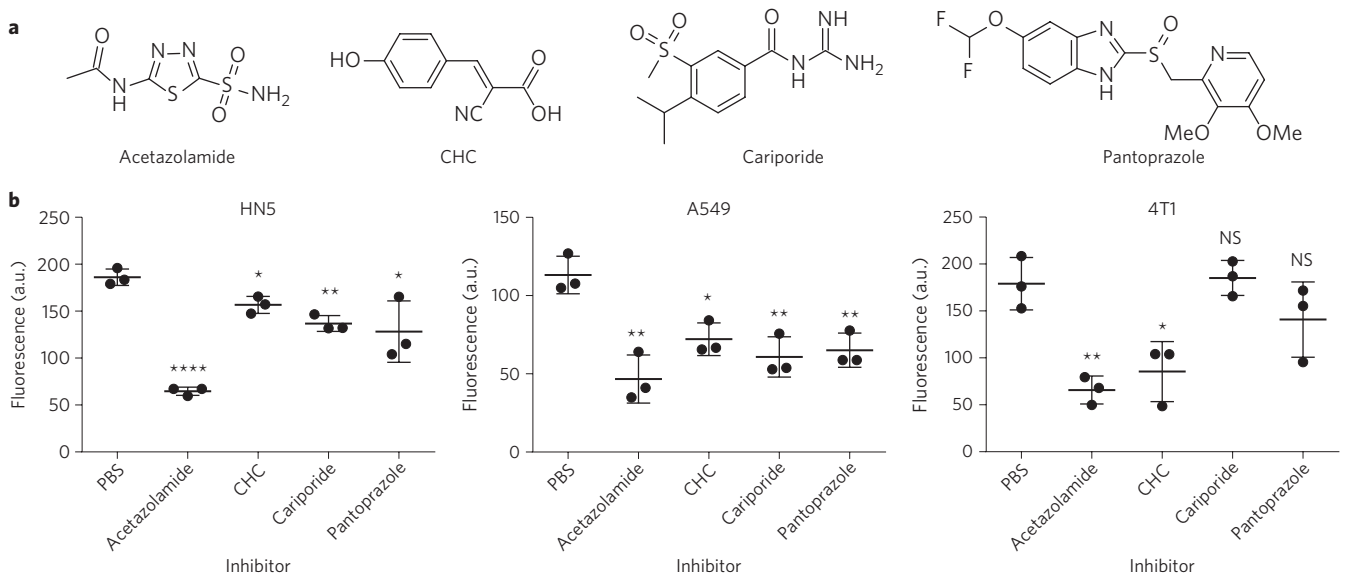

Figure 6 | PINS evaluation of small molecular inhibitors targeting different tumour acidosis pathways. a, Chemical structures of the small molecular inhibitors evaluated. **b**, Quantification of PINS signals in HN5, A549 and 4T1 tumour-bearing mice after injection of PBS or tumour-acidosis inhibitors. Corresponding NIR fluorescence images are shown in Supplementary Fig. 11. Data are presented as individual data points plus mean ± s.d ($n = 3$); $^{*}P < 0.05$, $^{**}P < 0.01$, $^{****}P < 0.0001$, NS = not significant.

biological signals into a discretized, binary output (Supplementary Fig. 9a). The significance of this conceptual realization became apparent when we performed numerous animal surgeries and were able to appreciate the consistency and robustness of the tumour signal. This level of consistency is rare in biology and was further confirmed when the current PINS included a simplified design without the need to introduce any targeting ligands (for example, cRGD, as in the previous study[15]) to achieve broad tumour imaging efficacy.

Our initial design of PINS with a threshold pH transition at 6.9 was created to maximally discretize the analogue acidic extracellular pH_e in tumours[14] (6.5–6.9, average 6.84) and normal tissue pH (7.4). Studies by ^{3}H-labelled PINS and fluorescence microscopy suggest that additional factors also contribute to the tumour contrast. For example, increased dose accumulation of PINS in HN5 tumours was found compared with muscle tissues (Supplementary Fig. 9b), which may be due to the enhanced permeability and retention effect in solid tumours[31]. It is worth noting that pH activation was able to further amplify the variable dose accumulation signal into discrete fluorescence signals between tumour and muscle tissues. In addition, fluorescence microscopy of tumour sections showed activated PINS in subcellular organelles, which may result from increased rates of macropinocytosis of cancer cells as a strategy to catabolize proteins for tumour growth and survival[32]. Internalization of PINS (either activated or intact) in acidic organelles such as lysosomes would keep the signal in the on state and also within the tumour cells rather than blurring the surrounding tissue through diffusion. This may explain the sustained imaging contrast over 24 h (Supplementary Fig. 4) as well as the sharp delineation of the tumour boundary from the surrounding muscle tissue (Supplementary Fig. 9a). Although the specific contribution from each input is unclear and may depend on the oncogenotypes of tumours, the transistor-like behaviour of PINS is able to combine the above contributions into an emergent and persistent tumour versus normal tissue signal. This ability of PINS, to use pH as a trigger to switch and amplify tumour signals, is unique from conventional pH sensors (for example, cell-impermeable 2-imidazole-1-yl-3-ethoxycarbonyl propionic acid (IEPA) and 3-aminopropylphosphonate (3-APP))[27] designed to measure the extracellular pH of solid tumours. Compared with these small molecular pH tracers, although PINS loses fine gradations of information (for example, the ability to differentiate pH 6.5 versus 6.8), its tradeoff is in the maximization of detection sensitivity by turning on and integrating all the pH signals below 6.9. This signal dichotomization strategy is essential towards achieving real-time image-guided surgery of solid tumours (Supplementary Videos 1–3) and the detection of small occult diseases (Fig. 5).

Surgical resection is a cornerstone of therapy for patients with solid cancers. For head and neck cancer, the complex mechanisms involved with speech and swallowing, the prevention of aspiration and the maintenance of the airway place a premium on surgical margins[33]. Breast-conserving lumpectomies are increasingly performed in 60–70% of patients. However, repeat surgery rates due to inadequate tumour removal are quite high (20–25%), especially in patients with larger tumours, positive axillary nodes, tumours with a lobular histology or those with an extensive intraductal component[34–37]. A variety of exogenous fluorophores have been developed for intraoperative margin assessment. Many of these agents are restricted to specific receptor expression profiles and thereby lack broad detection capabilities. Receptor-targeted imaging strategies are effective at stratifying patients towards therapy, but do not allow for the broad detection of tumours because of the large inter- and intra-tumour heterogeneity of solid tumours. By targeting a ubiquitous signal of cancer (dysregulated pH), PINS has shown broad tumour specificity for a variety of cancer types (head and neck, breast, kidney, pancreatic, brain and peritoneal metastasis) and in various mouse tumour models (transgenic, patient-derived xenograft and orthotopic xenograft). The high spatio–temporal sensitivity allowed real-time, image-guided surgery of head and neck tumours and breast tumours (Supplementary Videos 1–3), which significantly improved accuracy in the pathological validation of tumour margins (Fig. 4a). Achieving a tumour-free surgical margin with functional preservation of normal tissues is becoming an important objective during surgery. Based on the high-resolution capability of PINS in the delineation of tumour margins, we performed TAGS resection with >70% cures in head and neck tumour models and demonstrated the ability to remove small occult nodules in a triple negative breast cancer model. Accurate tumour margin delineation is a prerequisite for precise image-guided resection of tumours. Although most cancer surgeries do not require submillimetre resolution, real-time, high-resolution

visualization of tumours can still help decision-making in the operating room. This is particularly useful in the visualization of infiltrating lesions that were indeed detected in our experiments (Supplementary Video 1), where this additional detection was responsible for at least part of the observed survival differences as a result of TAGS compared with WLS (Fig. 4b).

In summary, the results from this study establish pH transistor nanoprobes as a broadly applicable strategy to allow highly sensitive, cancer-specific detection of malignant tumours. The ability of PINS to detect a range of tumours offers a broad image-guided strategy to improve tumour surgery. High-resolution, real-time delineation of tumours using clinical cameras have led to improved cancer detection and eradication in selected head and neck tumours and breast tumours. Key to this robust detection is the dichotomization of the output signal in response to a predetermined threshold in the input variable. This chemical digitization process removes ambiguity related to fluctuations or variability in the input biologic signal because of gating, which in turn minimizes noise. Potential challenges that may limit universal applicability of the nanoprobes in the clinics include a lack of fluorescence in benign, slow-growing or necrotic tumours and the physical limitation of light penetration in biological tissues. Nevertheless, we anticipate that this imaging paradigm will deliver broad impact in cancer staging, image-guided biopsy or surgery and will be used as a reporter assay for monitoring responses to drugs targeting tumour acidosis.

Methods

Synthesis and characterization of PINS. The EPA monomer was synthesized following the reported procedure[38]: 2-(ethylpropylamino)ethanol (26.2 g, 0.2 mol) and trimethylamine (27.9 ml, 0.2 mol) were dissolved in 200 ml dichloromethane and then methacryloyl chloride (19.4 ml, 0.2 mol) was added dropwise at 0 °C. The reaction was left overnight at room temperature. The solvent was removed by rotovap and the resulting residue was distilled *in vacuo* as a colourless liquid. The PEG-*b*-P(EPA$_x$-*r*-ICG$_y$) copolymer was synthesized using the atom transfer radical polymerization method[39]. In a typical procedure, EPA monomer (797.2 mg, 4 mmol), 2-aminoethyl methacrylate hydrochloride (50.0 mg, 0.3 mmol), *N*,*N*,*N*′,*N*″,*N*″-pentamethyldiethylenetriamine (PMDETA) (8.4 µl, 0.04 mmol) and MeO-PEG$_{114}$-Br (200.0 mg, 0.04 mmol) were charged into a polymerization tube. Then, a mixture of 2-propanol (1 ml) and dimethylformamide (DMF) (1 ml) was added to dissolve the monomer and initiator. After three cycles of freeze–pump–thaw to remove oxygen, CuBr (5.8 mg, 0.04 mmol) was added into the reaction tube under nitrogen atmosphere and the tube was sealed *in vacuo*. Polymerization was carried out at 40 °C for 12 h. After polymerization, the reaction mixture was diluted with 10 ml tetrahydrofuran (THF) and passed through an Al_2O_3 column to remove the catalyst. The THF solvent was removed by rotovap. The residue was dialyzed in distilled water and lyophilized to obtain a white powder. ICG was conjugated to the primary amino groups on the polymer via *N*-hydroxysuccinimide-ester chemistry[40]. The PINS nanoprobes were produced by a solvent evaporation method[15]. The final product was either concentrated to a 2.5 mg ml^{-1} aqueous stock solution for further usage or lyophilized for storage. TEM analysis was carried out on a JEOL 1200EX electron microscope. A Shimadzu ultraviolet–visible spectrophotometer (UV-1800 model) was used to determine the dye content in the ICG-conjugated polymer.

FDG–PET/computed tomography imaging. Animal protocol related to this study was reviewed and approved by the Institutional Animal Care and Use Committee and Radiation Safety Committee. Mouse FDG–PET/computed tomography (CT) imaging was performed using a Siemens Inveon PET/CT Multi-Modality System (Siemens Medical Solutions). All animals were fasted for 12 h prior to FDG–PET imaging. Each mouse received 5.55 MBq of FDG in 150 µl saline solution intravenously via a tail vein injection. The mice were placed on a heat pad before and during image acquisition. PET images were acquired 1 h post-injection, for 15 min, with animals under 2.5% isoflurane. PET images were reconstructed into a single frame using the 3D ordered subset expectation maximization (OSEM3D/MAP) algorithm. CT images were acquired immediately after PET. CT projections (360 steps per rotation) were acquired with a power of 80 kVp, current of 500 µA, exposure time of 145 ms, binning of 4 and effective pixel size of 102 µm. PET and CT images were co-registered by the manufacturer's software. Regions of interest were drawn manually over the tumour, guided by the corresponding CT images. The target activity was calculated as %ID g^{-1} tissue and the standardized uptake value (SUV) (Supplementary Table 4).

Fluorescence and tumour margin evaluation. Tumour and surrounding tissues were collected 24 h after probe injection. The collected samples were frozen in optimum cutting temperature (OCT) medium and 8 µm frozen section slides were prepared. The PINS fluorescence was imaged using a fluorescence flatbed scanner at 800 nm excitation (Odyssey, LI-COR Biosciences). GFP in the cancer cells were imaged with a Deltavision Deconvolution Microscope and images were stitched afterwards. H & E staining was performed after all fluorescent images were collected. The margins of the tumours were determined by a clinical pathologist (J.T.) from H & E staining. PINS fluorescent intensity and surrounding normal tissue fluorescence intensity were measured on the basis of five areas of interest (0.5 mm × 0.5 mm) for each sample.

Margin validation. Tissue specimens for margin validation were collected using a double blind protocol. Non-survival surgeries were performed with fluorescence guidance under a SPY Elite camera on nine head and neck tumour-bearing mice, following a similar procedure for survival surgery except that the mice were sacrificed after the surgery. The surgeon resected the tumours under PINS illumination and marked the tissue specimen (2–3 mm in size) as either primary tumour, tumour margin or negative muscle tissue, based on the fluorescence readings. For each tumour-bearing mouse, one tumour specimen, one tumour margin specimen and one negative tumour bed specimen were collected. Frozen sections were prepared from the specimens for H & E staining and histology validation. Histological evaluation was performed independently by a surgical pathologist without knowing the fluorescence assignment for each sample.

Survival surgery. Survival surgeries were performed in orthotopic HN5 head and neck cancer or 4T1 breast cancer models. All mice were injected with 2.0 mg kg^{-1} PINS 12–24 h prior to the surgery. For head and neck cancer surgery, the tumours were allowed to grow to 50 mm^3. Before surgery, all mice were randomized by an independent technician: each mouse was randomly picked up from the cage and assigned to control, debulking, WLS or TAGS group in sequence and the assignment was repeated until all groups reached the designated number of animals. Mice were then anaesthetized with 2.5% isoflurane. Hairs were removed with depilatory cream. Mice were prepped and draped in sterile fashion. For the debulking surgery group, the tumours were partially removed. For the WLS group, surgery was performed under white light illumination with the entire ascertainable tumour removed, based on the surgeon's best judgement. For the TAGS group, the surgery was performed with fluorescence guidance via a SPY Elite camera. White light illumination was left on for the TAGS group with no interference on the ICG imaging. After surgery, all animals received analgesic and antibiotics. Body weights were monitored before and after the surgery. Animals were examined for tumour recurrence three times a week. Animals were considered dead if the weight loss was more than 20% of the original body weight or the tumour volume exceeded 1,500 mm^3. For breast cancer surgery, 5×10^4 of 4T1 cells were injected into either the left or right inguinal mammary pad for tumour inoculation. For the TAGS group, the tumours were allowed to grow for four days after cancer cell injection. For the WLS group, the tumours were allowed to grow to a palpable size (25 mm^3). All animals without obvious signs of tumour recurrence were sacrificed on day 150 after surgery.

Tumour acidosis inhibition study. SCID mice bearing HN5 tumours of similar sizes were used to evaluate tumour responses to acidosis inhibitors. The mice were injected intravenously with PBS, acetazolamide (40 mg kg^{-1}), CHC (200 mg kg^{-1}), cariporide (25 mg kg^{-1}) or pantoprazole (50 mg kg^{-1}) 1 h before PINS (2.5 mg kg^{-1}) injection. Inhibitors except CHC were administrated again 6 h after PINS injection. Mice were imaged with a Hamamatsu PDE 24 h after probe injection. Tumour fluorescence intensities were measured by Image J and normalized to the PBS control.

Statistical analysis. Data are expressed as mean ± s.d. where $n \geq 5$ and plotted or tabulated as individual data points where $n < 5$. Sample sizes were chosen to ensure adequate power (>85%, at significance of 0.05) to detect predicted effect sizes, which were estimated on the basis of either preliminary data or previous experiences with similar experiments. The confidence interval of PINS detection accuracy was calculated using the exact method (one-sided). Differences between groups were assessed using unpaired, two-sided Student's *t*-tests for the calculation of *P* values. The Kaplan-Meier method was used to create survival function plots and *P* values comparing different survival groups were based on log-rank tests. Due to the very small number of multiple comparisons, *P* values are reported without adjustment. SAS 9.3 for Windows was used for data analysis.

Data availability. All the data supporting the findings of this study are available within the paper and its Supplementary Information.

Received 18 June 2016; accepted 8 November 2016; published 19 December 2016

References

1. Vogelstein, B. *et al.* Cancer genome landscapes. *Science* **339,** 1546–1558 (2013).
2. van Dam, G. M. *et al.* Intraoperative tumor-specific fluorescence imaging in ovarian cancer by folate receptor-alpha targeting: first in-human results. *Nat. Med.* **17,** 1315–1319 (2011).

3. Veiseh, M. *et al.* Tumor paint: a chlorotoxin:Cy5.5 bioconjugate for intraoperative visualization of cancer foci. *Cancer Res.* **67,** 6882–6888 (2007).
4. Ke, S. *et al.* Near-infrared optical imaging of epidermal growth factor receptor in breast cancer xenografts. *Cancer Res.* **63,** 7870–7875 (2003).
5. Koyama, Y. *et al.* Spectral fluorescence molecular imaging of lung metastases targeting HER2/neu. *Clin. Cancer Res.* **13,** 2936–2945 (2007).
6. Nakajima, T. *et al.* Targeted, activatable, *in vivo* fluorescence imaging of prostate-specific membrane antigen (PSMA) positive tumors using the quenched humanized J591 antibody-indocyanine green (ICG) conjugate. *Bioconjug. Chem.* **22,** 1700–1705 (2011).
7. Jacobs, T. W., Gown, A. M., Yaziji, H., Barnes, M. J. & Schnitt, S. J. HER-2/neu protein expression in breast cancer evaluated by immunohistochemistry. A study of interlaboratory agreement. *Am. J. Clin. Pathol.* **113,** 251–258 (2000).
8. Paik, S. *et al.* HER2 and choice of adjuvant chemotherapy for invasive breast cancer: national surgical adjuvant breast and bowel project protocol B-15. *J. Natl Cancer Inst.* **92,** 1991–1998 (2000).
9. Hanahan, D. & Weinberg, R. A. Hallmarks of cancer: the next generation. *Cell* **144,** 646–674 (2011).
10. Heiden, M. G. V., Cantley, L. C. & Thompson, C. B. Understanding the Warburg effect: the metabolic requirements of cell proliferation. *Science* **324,** 1029–1033 (2009).
11. Zhu, A., Lee, D. & Shim, H. Metabolic positron emission tomography imaging in cancer detection and therapy response. *Semin. Oncol.* **38,** 55–69 (2011).
12. Webb, B. A., Chimenti, M., Jacobson, M. P. & Barber, D. L. Dysregulated pH: a perfect storm for cancer progression. *Nat. Rev. Cancer* **11,** 671–677 (2011).
13. Gillies, R. J., Raghunand, N., Garcia-Martin, M. L. & Gatenby, R. A. pH imaging. A review of pH measurement methods and applications in cancers. *IEEE Eng. Med. Biol.* **23,** 57–64 (2004).
14. Volk, T., Jahde, E., Fortmeyer, H. P., Glusenkamp, K. H. & Rajewsky, M. F. pH in human tumour xenografts: effect of intravenous administration of glucose. *Br. J. Cancer* **68,** 492–500 (1993).
15. Wang, Y. *et al.* A nanoparticle-based strategy for the imaging of a broad range of tumours by nonlinear amplification of microenvironment signals. *Nat. Mater.* **13,** 204–212 (2014).
16. Zhou, K. *et al.* Multicolored pH-tunable and activatable fluorescence nanoplatform responsive to physiologic pH stimuli. *J. Am. Chem. Soc.* **134,** 7803–7811 (2012).
17. Li, Y. *et al.* Molecular basis of cooperativity in pH-triggered supramolecular self-assembly. *Nat. Commun.* **7,** 13214 (2016).
18. Bardeen, J. Research leading to point-contact transistor. *Science* **126,** 105–113 (1957).
19. Cook, G. J., Wegner, E. A. & Fogelman, I. Pitfalls and artifacts in 18FDG PET and PET/CT oncologic imaging. *Semin. Nucl. Med.* **34,** 122–133 (2004).
20. Fukui, M. B. *et al.* Combined PET–CT in the head and neck: part 2. Diagnostic uses and pitfalls of oncologic imaging. *Radiographics* **25,** 913–930 (2005).
21. Neri, D. & Supuran, C. T. Interfering with pH regulation in tumours as a therapeutic strategy. *Nat. Rev. Drug Discov.* **10,** 767–777 (2011).
22. Sonveaux, P. *et al.* Targeting lactate-fueled respiration selectively kills hypoxic tumor cells in mice. *J. Clin. Invest.* **118,** 3930–3942 (2008).
23. Cardone, R. A., Casavola, V. & Reshkin, S. J. The role of disturbed pH dynamics and the Na+/H+ exchanger in metastasis. *Nat. Rev. Cancer* **5,** 786–795 (2005).
24. Vishvakarma, N. K. & Singh, S. M. Mechanisms of tumor growth retardation by modulation of pH regulation in the tumor-microenvironment of a murine T cell lymphoma. *Biomed. Pharmacother.* **65,** 27–39 (2011).
25. Lou, Y. *et al.* Targeting tumor hypoxia: suppression of breast tumor growth and metastasis by novel carbonic anhydrase IX inhibitors. *Cancer Res.* **71,** 3364–3376 (2011).
26. Pacchiano, F. *et al.* Ureido-substituted benzenesulfonamides potently inhibit carbonic anhydrase IX and show antimetastatic activity in a model of breast cancer metastasis. *J. Med. Chem.* **54,** 1896–1902 (2011).
27. Gillies, R. J., Raghunand, N., Karczmar, G. S. & Bhujwalla, Z. M. MRI of the tumor microenvironment. *J. Magn. Reson.* **16,** 430–450 (2002).
28. Gallagher, F. A. *et al.* Magnetic resonance imaging of pH *in vivo* using hyperpolarized 13C-labelled bicarbonate. *Nature* **453,** 940–943 (2008).
29. Parks, S. K., Chiche, J. & Pouyssegur, J. Disrupting proton dynamics and energy metabolism for cancer therapy. *Nat. Rev. Cancer* **13,** 611–623 (2013).
30. Ang, K. K. *et al.* Impact of epidermal growth factor receptor expression on survival and pattern of relapse in patients with advanced head and neck carcinoma. *Cancer Res.* **62,** 7350–7356 (2002).
31. Maeda, H., Wu, J., Sawa, T., Matsumura, Y. & Hori, K. Tumor vascular permeability and the EPR effect in macromolecular therapeutics: a review. *J. Control. Release* **65,** 271–284 (2000).
32. Commisso, C. *et al.* Macropinocytosis of protein is an amino acid supply route in Ras-transformed cells. *Nature* **497,** 633–637 (2013).
33. More, Y. I. *et al.* Functional swallowing outcomes following transoral robotic surgery vs primary chemoradiotherapy in patients with advanced-stage oropharynx and supraglottis cancers. *JAMA Otolaryngol. Head Neck Surg.* **139,** 43–48 (2013).
34. Anscher, M. S. *et al.* Local failure and margin status in early-stage breast carcinoma treated with conservation surgery and radiation therapy. *Ann. Surg.* **218,** 22–28 (1993).
35. Schmidt-Ullrich, R. *et al.* Tumor margin assessment as a guide to optimal conservation surgery and irradiation in early stage breast carcinoma. *Int. J. Radiat. Oncol.* **17,** 733–738 (1989).
36. Solin, L. J., Fowble, B. L., Schultz, D. J. & Goodman, R. L. The significance of the pathology margins of the tumor excision on the outcome of patients treated with definitive irradiation for early stage breast cancer. *Int. J. Radiat. Oncol.* **21,** 279–287 (1991).
37. Holland, R. *et al.* The presence of an extensive intraductal component following a limited excision correlates with prominent residual disease in the remainder of the breast. *J. Clin. Oncol.* **8,** 113–118 (1990).
38. Zhou, K. *et al.* Tunable, ultrasensitive pH-responsive nanoparticles targeting specific endocytic organelles in living cells. *Angew. Chem. Int. Ed.* **50,** 6109–6114 (2011).
39. Matyjaszewski, K. & Tsarevsky, N. V. Nanostructured functional materials prepared by atom transfer radical polymerization. *Nat. Chem.* **1,** 276–288 (2009).
40. Ma, X. *et al.* Ultra-pH-sensitive nanoprobe library with broad pH tunability and fluorescence emissions. *J. Am. Chem. Soc.* **136,** 11085–11092 (2014).

Acknowledgements

This work was supported by the National Institutes of Health (R01EB013149 and R01CA192221, to J.G.) and Cancer Prevention and Research Institute of Texas (RP140140, to B.D.S. and J.G.). Animal imaging work was supported by the UT Southwestern Small Animal Imaging Resource Grant (U24 CA126608) and Simmons Cancer Center Support Grant (P30 CA142543). We thank J. Sun for animal imaging, L.C. Su for histology analysis, D. Zhao for preparation of the U87 brain tumour model, A. Pavia-Jimenez and J. Brugarolas for the renal PDX model and G. Balch for the peritoneal metastatis model.

Author contributions

T.Z., B.D.S and J.G. are responsible for all phases of the research. G.H., S.Y., M.L. and Z.Z. assisted animal surgery, tumour-margin analysis and safety evaluation. Y.L. helped develop the transistor concept and performed TEM analysis. S.R. and X.K.S. designed the FDG–PET experiment and performed image analysis. Z.Q.L. performed the imaging comparison of PINS with other commercial probes. Y.G.W. and E.B. helped with fluorescence imaging and X.P.M. assisted with the design and synthesis of the PEPA polymer. B.D.S. and T.Z. performed the survival surgery in mice bearing head and neck cancer, and breast cancer, respectively. X.J.X. performed the statistical analysis. J.T. interpreted the histology slides. R.A.B. helped establish genetic pancreatic models and histology interpretations.

Additional information

Supplementary information is available for this paper.

Reprints and permissions information is available at www.nature.com/reprints.

Correspondence and requests for materials should be addressed to B.D.S. or J.G.

How to cite this article: Zhao, T. *et al.* A transistor-like pH nanoprobe for tumour detection and image-guided surgery. *Nat. Biomed. Eng.* **1,** 0006 (2016).

Competing interests

B.D.S. and J.G. are scientific co-founders of OncoNano Medicine, Inc.